Received: 20 June 2021 | Accepted: 25 October 2021

DOI: 10.1002/maco.202112615

ARTICLE

Materials and Corrosion

Hydrogen uptake and diffusivity in steel armor wires with different chemical composition, carbide distribution, grain size, and degree of deformation

Ellen S. Skilbred[1] | **Mariano Kappes**[2] | **Mariano Iannuzzi**[1,3] | **Roy Johnsen**[1]

[1]Department of Mechanical and Industrial Engineering, Norwegian University of Science and Technology, Trondheim, Norway

[2]Instituto Sabato, San Martín, Buenos Aires, Argentina

[3]Curtin Corrosion Centre, Curtin University, Perth, Western Australia, Australia

Correspondence
Ellen S. Skilbred, Department of Mechanical and Industrial Engineering, Norwegian University of Science and Technology, 7034 Trondheim, Norway.
Email: ellen.s.skilbred@ntnu.no

Funding information
The Research Council of Norway, Grant/Award Number: 280760

Abstract

In this study, six flexible pipe steel armor wires used in oil and gas transportation are characterized, and their hydrogen diffusion coefficients and hydrogen uptakes are measured using an electrochemical hydrogen permeation technique. The wires have ferritic–pearlitic microstructures with round, lamellar, or partially lamellar carbides and the shape and orientation of the grains indicate that the microstructures were plastically deformed to different degrees. It was assumed that hydrogen was transported through the ferrite, so the presence of cementite in the steel armor wires leads to longer hydrogen diffusion paths through the ferrite, which was quantified with a tortuosity factor. After compensating for tortuosity, the normalized steady-state flux shows a tendency to increase as the grain size decreases. The effective diffusion coefficients increase with a decrease of the ferrite–cementite interface area, suggesting trapping on the ferrite–cementite interfaces. The uptake of diffusible hydrogen was lowest for the least plastically deformed materials and about twice as high for the more plastically deformed materials.

KEYWORDS
carbide distribution, deformation, diffusivity, hydrogen, steel armor wires

1 | INTRODUCTION

Flexible pipes are frequently used for oil and gas transportation. Each pipe consists of several layers with specific purposes that combined give the desired mechanical and chemical resistance required for the designed operating conditions. Many designs are possible, but usually, the pipes comprise five main unbonded layers: a carcass made of a corrosion-resistant alloy closest to the bore, a polymer sheath, a pressure armor layer made of steel, a tensile armor layer made of high strength steel wires, and an outer polymer sheath.[1,2] The annulus around the tensile armor wires is dry under normal operating conditions but can be flooded with condensed water containing corrosive species like CO_2, H_2S, or both, which permeate from the bore, and seawater when there are damages in the outer polymer sheath. The resulting exposure to corrosive media can lead to corrosion and hydrogen embrittlement (HE) of the tensile wires.[1–4] In this regard, both corrosion and cathodic protection (when the outer shielding is damaged) may introduce atomic hydrogen to the wires.

Several incidents of brittle fractures and severe corrosion attacks of flexible pipe steel armor wires have been reported[5–7] and the failure mechanism can be complex. Understanding the relationship between hydrogen uptake and microstructure in the armor wires is a crucial step towards understanding the complex failure mechanisms of flexible pipes and improving flexible pipe design.

HE is caused by the presence of hydrogen within an alloy or metal.[8] In carbon and low alloy steels, the presence of atomic hydrogen can induce premature failures by interactions with dislocation formation and movement, decreasing the cohesion between atoms in the lattice, and interaction with local stress and strain fields.[9] Some microstructural sites have a higher affinity to hydrogen than the interstitial lattice sites and serve as hydrogen traps. Hydrogen traps are often divided into reversible and irreversible, according to the hydrogen desorption probability at room temperature.

Given the very low probability of hydrogen desorption from irreversible traps, they can be saturated even when the hydrogen concentration in the material is low, whereas reversible traps can reach dynamic equilibrium with the hydrogen in the lattice. Grain and phase boundaries, vacancies, inclusions, and dislocations are all examples of typical trapping sites in steels.[10] Findley et al.[11] summarized the binding energy of several types of traps from 18 references and reported that the binding energy of dislocations was 18–59.9 kJ mol^{-1}, grain boundaries 8.8–58.9 kJ mol^{-1}, voids 29.1 kJ mol^{-1}, and ferrite–cementite interface 8.4–15.7 kJ mol^{-1}. These are all considered reversible traps. The hydrogen in lattice and reversible traps—also referred to as diffusible hydrogen—has a more severe impact on mechanical properties than the irreversibly trapped hydrogen since the diffusible hydrogen can accumulate in regions with high stress and facilitate crack initiation and propagation.[9,12]

There is a substantial body of research on the effect of different parameters on the HE susceptibility of steels where the microstructures were carefully controlled to investigate the effect of changing one parameter at a time.[13–21] However, there is limited work on the interplay between armor wire steel microstructure and hydrogen to date. In this paper, the HE susceptibility of materials with complex microstructures is investigated, and the difference in hydrogen diffusivity, permeation flux, and uptake is discussed based on several differences in microstructural features. Six types of flexible pipe armor steel wire were tested using electrochemical hydrogen permeation experiments. The work focuses on estimating the diffusible hydrogen content since this is the most detrimental in cases where there is a constant supply of hydrogen, like during a corrosion process or cathodic protection of a flooded flexible pipe annulus. A detailed metallographic study was conducted to compare the microstructures of the wires and to distinguish between the effect of hydrogen trapping and tortuous hydrogen diffusion paths on the effective diffusion coefficients. The wires tested were qualified according to the API 17J Specification for Unbonded Flexible Pipe[22] for different operating conditions, as discussed below. The outcome of this investigation will support future considerations regarding the replacement and lifetime extension of flexible pipes.

2 | EXPERIMENTAL

2.1 | Materials

Six types of flexible pipe wires qualified for different operating conditions were provided and are identified by letters A–F. The wire materials complied with API 17J and were delivered in their service thermo-mechanical condition. Samples were taken from coils, and some pieces were straightened using a roller straightener to fit the required dimensions of the electrochemical permeation cell. The thickness of the wires was 3 mm, and the widths ranged from 9 to 12 mm. The chemical compositions of the wires are given in Table 1. Scanning electron microscopy (SEM) images of the center of the cross-sections of the six materials are given in Figure 1. The surfaces in the images were prepared as described in Section 2.2. Images at a higher magnification can be consulted in Figure 2 for Materials D and E. All the wires had features associated with rolled microstructures, with grains being narrower through-thickness than in the width and length directions. The exact thermo-mechanical fabrication route of these materials was not available, but the size and shape of ferrite provided insight on whether the wires were subjected to long heat treatments after the rolling process. The wires' extent of plastic deformation, the estimated grain size, and the cementite morphology are described in Table 2 with the hardness, yield strength, ultimate tensile strength, and plastic strain-to-failure (Ep). The Ep was calculated according to NACE Standard TM0198-2016.[23] The materials have complex microstructures with many unclear grain boundaries and the grain size is therefore described by the largest well-defined grains observed instead of average grain size. The ferrite and cementite grains were of different sizes and are therefore evaluated separately.

TABLE 1 Cementite fractions (f) and chemical compositions of the wire materials

Material	f	C (wt%)	Si (wt%)	S (wt%)	P (wt%)	Mn (wt%)	Ni (wt%)	Cr (wt%)	Al (wt%)
A	0.077	0.501	0.247	0.002	0.003	0.604	0.001	0.011	0.031
B	0.043	0.282	0.223	0.010	0.006	0.733	0.010	0.003	0.035
C	0.054	0.353	0.194	0.007	0.009	0.678	0.013	0.003	0.042
D	0.127	0.830	0.331	0.005	0.005	0.683	0.005	0.002	0.041
E	0.095	0.618	0.225	0.002	0.007	0.729	0.009	0.032	0.037
F	0.100	0.651	0.240	0.009	0.002	0.630	0.060	0.025	0.003

Material	V (wt%)	Pb (wt%)	N (wt%)	Ti (wt%)	Sn (wt%)	Cu (wt%)	Co (wt%)	Mo (wt%)	B (wt%)
A	0.036	0.050	0.009	$<10^{-4}$	N.D.	N.D.	N.D.	0.001	$<10^{-4}$
B	0.001	0.065	0.020	0.002	N.D.	$<10^{-4}$	$<10^{-4}$	0.001	$<10^{-4}$
C	0.002	0.065	0.219	0.002	$<10^{-3}$	0.001	N.D.	0.001	$<10^{-4}$
D	0.050	0.065	0.099	0.004	0.001	$<10^{-4}$	N.D.	0.002	$<10^{-3}$
E	0.001	0.050	0.014	$<10^{-4}$	N.D.	N.D.	N.D.	$<10^{-3}$	$<10^{-4}$
F	0.001	0.040	0.009	N.D.	N.D.	$<10^{-3}$	0.001	$<10^{-4}$	$<10^{-4}$

Note: Elements that were not detected for a particular material are labeled with N.D.

Abbreviations: Ep, plastic strain-to-failure; UTS, ultimate tensile strength; YS, yield strength.

2.2 | Metallographic preparation and analysis

The microstructure of the materials was examined using SEM images. Before SEM imaging, the surfaces were ground to European grit P4000, polished to 1 μm diamond suspension, and etched in 2 vol% Nital solution for 5–6 s. The Nital solution was prepared by adding 2 ml of 67–70 wt% HNO_3 into 100 ml of ethanol.

The ferrite–cementite interfacial area, S_v, the mean free path between cementite particles, λ_p, and the mean true spacing for lamellar materials, σ_0, were calculated as described by Johnson and Krauss;[13] $S_v = 4N$ where N is the number of particles or platelets intercepted per unit of length of a test line, $\lambda_p = (1-f)/N$, where f is the volume fraction of cementite, calculated with the lever rule and assuming all C is located in cementite, Fe_3C, and $\sigma_0 = 2/S_v$. For each material, N was determined from four images of the middle of cross-sections and four images in the middle of the wires in the width-length plane. Five horizontal and five vertical test lines were measured for each image, that is, 20 lines were used to find the average number of cementite interceptions on the test lines in the thickness and length directions while 40 lines were used to find the average number of cementite interceptions in the width direction. SEM images with magnifications varying from ×5000 to ×50 000 were used, depending on the grain size and size of lamellas or cementite particles. All materials were evaluated at ×20 000 and at least one other magnification.

The tortuosity of the hydrogen diffusion path in the electrochemical hydrogen permeation experiments was determined by examining cross-section micrographs. In the electrochemical hydrogen permeation experiments, hydrogen diffuses in the direction of the thickness, and the tortuosity was therefore only studied in through-thickness. Image analyses were first conducted by examining micrographs from three positions in the cross-sections at ×10 000. One to three images were analyzed for each position. For each image, a red line was drawn from side to side, in the direction of diffusion during electrochemical permeation tests, and the number of red pixels was divided by the number of pixels between the two sides of the image. An example is shown in Figure 3. The red line was chosen to start at a point where it was clear that the shortest path of diffusion was seen inside the image. Each line was drawn straight until it reached a particle or lamella, then the necessary steps were taken to avoid the obstacle and before it continued in a straight line. The number of pixels in a line was then equal to the number of pixels from one side of the image to the other plus the number of extra pixels drawn to overcome obstacles. For some images, especially the ones with spheroidized carbides, several lines could be drawn without the lines going through the same grains. The same

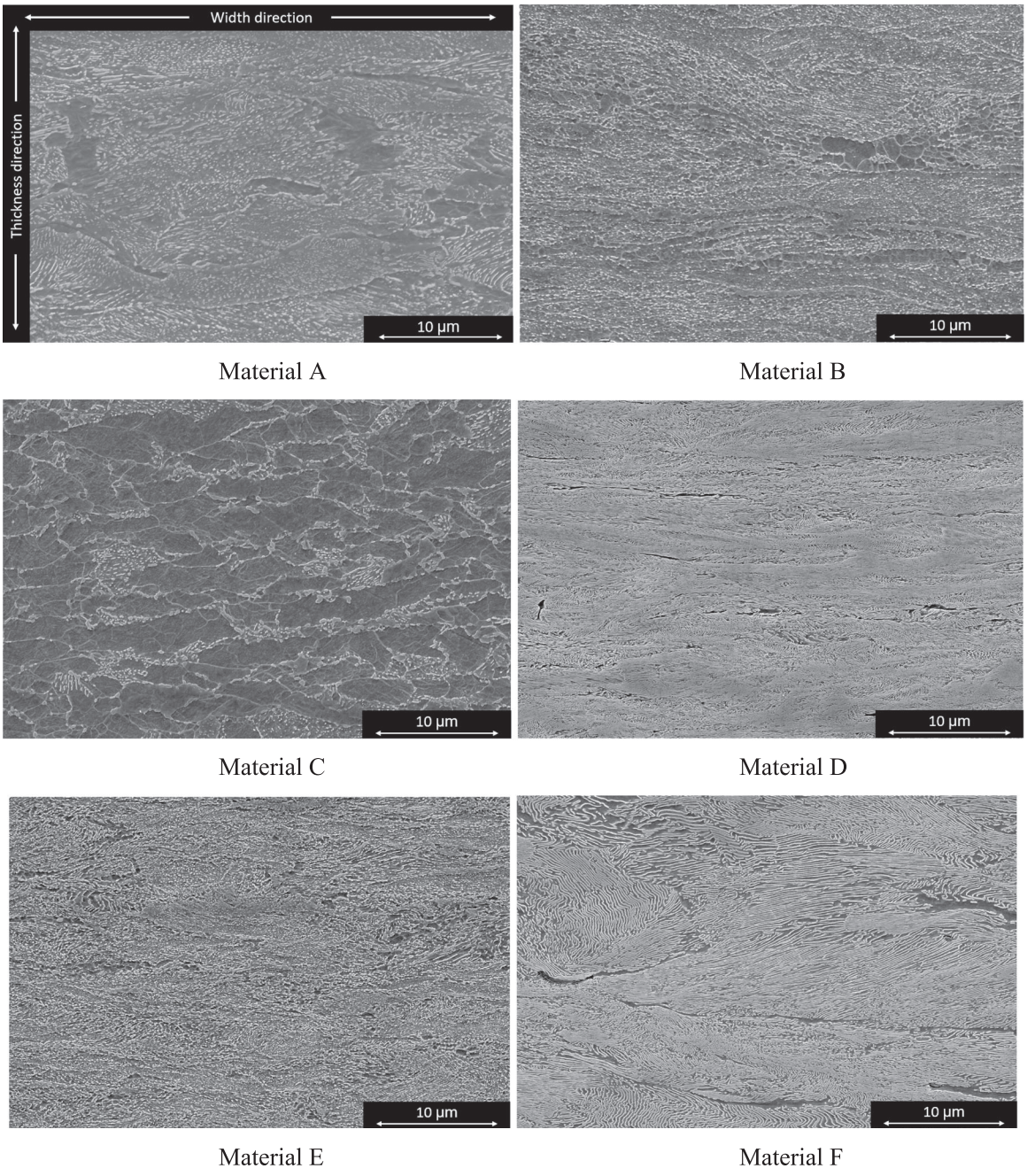

FIGURE 1 Scanning electron microscopy images illustrating the microstructure of the wires, as indicated. The orientation of the images is indicated in the image of Material A

image was then sometimes used to find two lines. All the materials had at least two lines drawn for each of the three positions. More images were analyzed for the materials with the highest data variance. This method has been shown sensitive to the image resolution, and the first screening was therefore conducted with images in the same magnification for all the materials. A second screening was conducted for Materials D and F, where Material D was evaluated at ×20 000 and Material F at ×5000. The images were distributed more evenly around the cross-section in the second screening.

2.3 | Electrochemical hydrogen permeation experiments

The hydrogen uptake and diffusion coefficients of the materials were determined by electrochemical hydrogen permeation experiments, similar to the experimental configuration described by Devanathan and Stachurski.[24] The cell consisted of two compartments separated by the steel specimen in the middle. The principle behind the method is to charge the sample with hydrogen on one side and detect

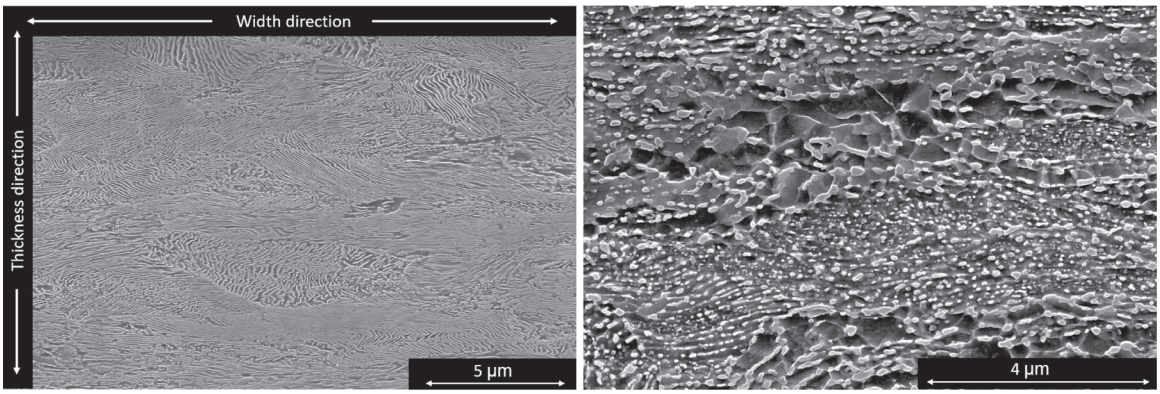

FIGURE 2 Scanning electron microscopy images of Materials D and E

TABLE 2 Mechanical and microstructural properties of the wire materials

Material	Extent of plastic deformation	Cementite morphology
A	Some deformation	Globular, partly lamellar
B	Pearlite deformed. Some banding of ferrite	Globular
C	Some banding and deformation	Globular
D	Highly deformed grains	Lamellar
E	Pearlite deformed. Some banding of ferrite	Globular, partly lamellar
F	Some deformation of pearlite. Ferrite heavily deformed	Lamellar

	Estimated grain size					
Material	Ferrite (µm)	Cementite (µm)	Hardness (HV_{10})	YS (MPa)	UTS (MPa)	Ep
A	≤14	≤36	331 ± 14	871	1009	0.115
B	≤10	≤28	290 ± 10	805	847	0.157
C	≤20	≤14	257 ± 4	616	744	0.152
D	≤7	≤24	453 ± 16	1408	1622	0.094
E	≤3	≤22	386 ± 8	1097	1260	0.108
F	≤20	≤32	384 ± 6	1252	1408	0.099

Abbreviations: Ep, plastic strain-to-failure; UTS, ultimate tensile strength; YS, yield strength.

electrochemically the hydrogen that has diffused through the specimen on the opposing side, Figure 4.

2.3.1 | Sample preparation

Since the microstructures of the wires were anisotropic, it was decided to keep the materials in their original thickness, although some material was lost due to grinding. The sample thicknesses ranged from 2.54 to 2.85 mm, ideally leading to a circular exposed area of 28.5 mm radius to fulfill the desired minimum 10:1 radius-to-thickness ratio, as recommended by ISO 17081[25] and ASTM G148[26] to guarantee one- dimensional (1D) diffusion through the thickness. Maintaining the preferred radius was not possible since the width of the wire was 12 mm or smaller. Thus, the wires were embedded in a light-curing resin (Technovit® LC 2000) mixed with its optional additive "Inside Cure" to maximize the exposed area. An embedded sample is shown in Figure 5. All sample sides were ground with SiC paper, washed in acetone, and sonicated in ethanol before mounting. The two sides exposed in the permeation cell were ground to European grit P1200 SiC paper before the samples were heated to 120°C in a heating cabinet overnight, to reveal sites with bad adhesion between the steel and embedding. Any sites with poor adhesion between the polymer and steel were visible after heating and only defect-free samples were used in the tests. Before exposure in the test cell, the samples were coated

with palladium on one side by electrodeposition according to the procedure proposed by Bruzzoni[27] and described in detail by Husby et al.[14] After the samples were coated with Pd, they were heated to 120°C in a heating cabinet for at least 16 h to remove any hydrogen that may have been absorbed by the samples during the Pd-coating process and diffused to irreversible traps. This procedure was used by Rivera et al.[28] who exposed the samples to 110°C. In the absence of a palladium coating on the hydrogen exit side (i.e., anodic side), the steady-state permeation current can decrease with time.[29–31] This drop in steady-state permeation current may be acceptable for experiments expected to last a few hours, but for the thick samples used in this study, a palladium coating on the hydrogen exit side was considered necessary. The hydrogen entry side was left uncoated and re-ground with European grit P1200 SiC paper, rinsed in distilled water, and dried with hot air just minutes before the electrochemical hydrogen permeation experiments.

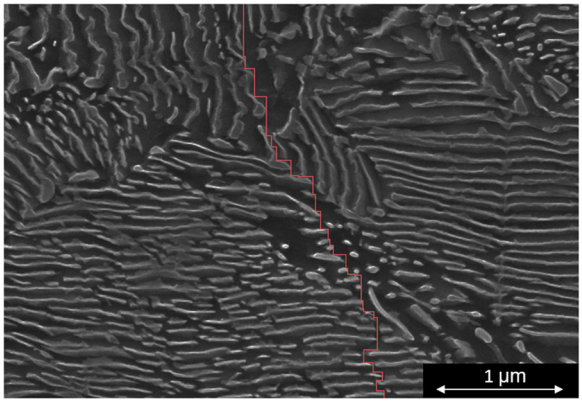

FIGURE 3 Example of a line drawn to estimate the tortuosity of the hydrogen diffusion path in Material F. The image is shown here is cropped and magnified to improve the visibility [Color figure can be viewed at wileyonlinelibrary.com]

2.3.2 | Measurement of hydrogen permeation transients

The sample was placed in the sample holder and the screw was inserted to make electrical contact, as shown in Figure 4. Gaskets were placed on both sides of the sample before the glass compartments and the clamping system was mounted around the sample. Both compartments of the cell were filled with 0.1 M NaOH and constantly purged with nitrogen gas to remove oxygen, as recommended for carbon steels in ISO 17081.[25] Each compartment had mercury–mercurous electrode (MME) ($Hg/Hg_2SO_4/SO_4^{2-}$) in saturated K_2SO_4 solution as a reference and a platinum wire as a counter electrode. The potential of the MME electrode is +650 mV versus the normal hydrogen electrode. Hydrogen was introduced by galvanostatic polarization using an applied

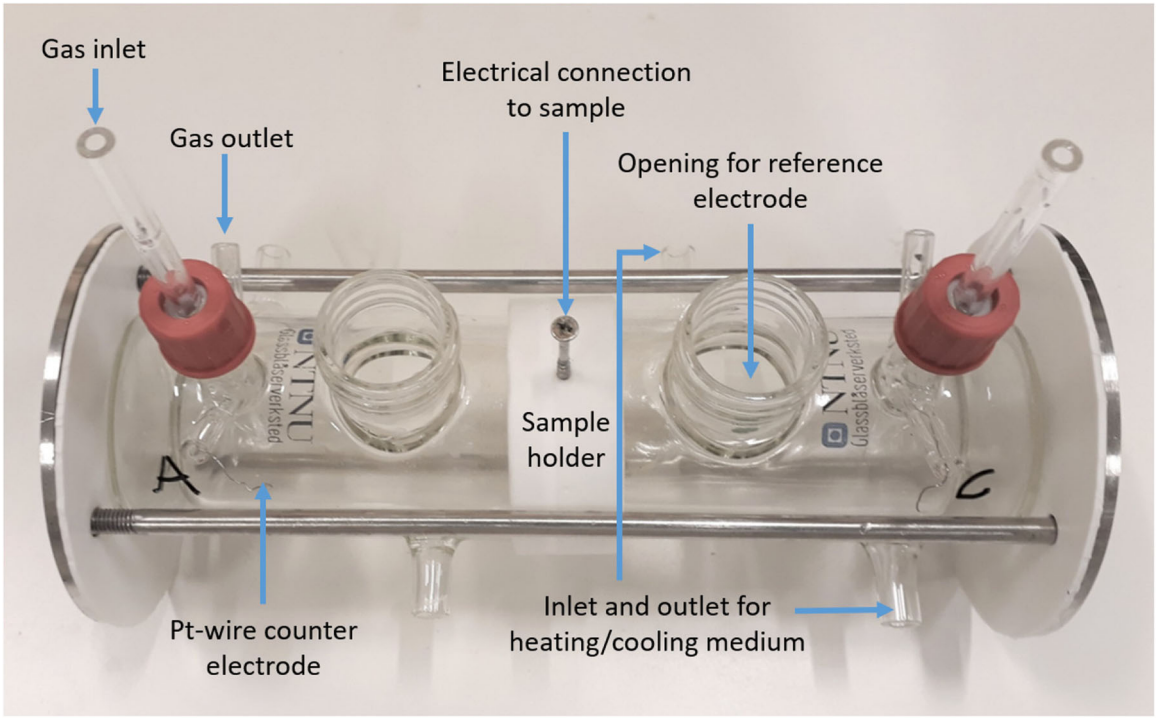

FIGURE 4 Electrochemical hydrogen permeation cell [Color figure can be viewed at wileyonlinelibrary.com]

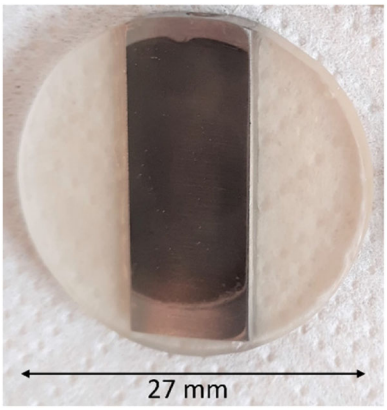

FIGURE 5 Electrochemical hydrogen permeation sample. The translucent part of the sample is the embedding. The dark area of the sample was coated with Pd and exposed facing the anodic side of the hydrogen permeation cell [Color figure can be viewed at wileyonlinelibrary.com]

current, $i_{app} = -12\ mA\ cm^{-2}$. This compartment will be described as the cathodic compartment and the corresponding side of the sample as the cathodic side. In the other compartment, that is, the exit or anodic compartment, the sample was anodically polarized to −110 mV versus MME (+300 mV vs. SCE or +340 mV vs. Ag/AgCl sat. KCl). The experiments started with stabilizing the surfaces in both compartments to −110 mV versus MME until the current on the anodic side was lower than $0.1\ \mu A\ cm^{-2}$. Then, galvanostatic charging started on the cathodic side. When hydrogen reached the anodic side, the current increased until steady-state diffusion was reached and the current on the anodic side stabilized. The galvanostatic charging was then stopped and hydrogen removed from the test sample by anodic polarization at −110 mV vs. MME on both sides, which is referred to as discharging or decay transient. When the anodic side reached a current density below $0.1\ \mu A\ cm^{-2}$, the galvanostatic charging was re-started and the new hydrogen charging transient was measured. A second decay transient was recorded after steady-state diffusion was reached. Water at 25 ± 1°C was circulated through the jacket of the anodic and cathodic compartments of the cell.

2.3.3 | Analysis of the results

The electrochemical hydrogen permeation experiment is designed to have 1D hydrogen diffusion, a linear gradient of lattice hydrogen concentration in the material at a steady state, and a diffusible hydrogen concentration equal to zero on the anodic side.[25,26] It is assumed that during steady-state permeation, the hydrogen traps are occupied and in equilibrium with the lattice concentration so that lattice hydrogen diffusion dominates. There may be obstacles to hydrogen diffusion through which hydrogen cannot diffuse.[32] Cementite is considered to be an example of this kind of obstacle for hydrogen diffusion, besides contributing to increased hydrogen uptake by trapping on the cementite–ferrite interfaces.[13,33] Hydrogen diffusion inside any cementite phase in ferritic–pearlitic steels can therefore be neglected. Thus, hydrogen diffusion in the lattice during steady-state is expected to be governed by the theoretical diffusion coefficient of ferrite, D_l. The permeation flux at steady-state, J_{SS}, depends on the length of the hydrogen pathway through the sample, L, and the subsurface concentration of hydrogen in lattice sites at the entry side, C_0. Since the lattice hydrogen is expected to be present mainly in ferrite and the materials contain both ferrite and cementite, the subsurface concentration of hydrogen is denoted C_0^{av} here, to emphasize that the concentration is based on the assumption of equal distribution of lattice hydrogen over the hydrogen entry surface.[34]

$$J_{SS} = \frac{D_l C_0^{av}}{L}. \tag{1}$$

C_0^{av} must be divided by the volume fraction of ferrite to find the subsurface concentration of lattice hydrogen in the ferrite phase, C_0^{Fe}.[34]

$$C_0^{Fe} = \frac{C_0^{av}}{1\text{-}f} \tag{2}$$

Similarly, J_{SS} reflects the average flux of hydrogen while J_{SS}^{Fe} is introduced to quantify the flux of hydrogen in the ferrite phase, assuming no hydrogen flux in the cementite

$$J_{SS}^{Fe} = \frac{D_l C_0^{Fe}}{L} = \frac{J_{SS}^{av}}{1-f}. \tag{3}$$

In the range −40°C to 80°C, D_l for ferrite is given by[35]

$$D_l = 7.23 \times 10^{-8} \exp\left(\frac{-Q}{RT}\right) m^2 s^{-1} \tag{4}$$

where $Q = 5.69\ kJ\ mol^{-1}$ and R is the gas constant $8.314\ J\ K^{-1}\ mol^{-1}$. This gives $D_l = 7.28 \times 10^{-5}\ cm^2\ s^{-1}$ at 25°C. When only reversible trapping sites are present and the trap occupancy is low, the concentration of hydrogen in lattice and reversible trapping sites, C_{0R}, can be estimated by reformulating Equation (1) and using the effective diffusion coefficient, D_{eff}, which accounts for the effect of trapping on diffusivity.[25]

$$C_{0R} = \frac{J_{SS}L}{D_{eff}} = \frac{I_{SS}L}{A_{surface}FD_{eff}}. \quad (5)$$

Here, I_{SS} is the steady-state permeation current measured on the anode side, $A_{surface}$ is the exposed surface area, and F is Faraday's constant equal to 96485 C mol^{-1}. D_{eff} can be determined in several ways. One way is to use the breakthrough time, t_b, which is determined by extrapolating the linear portion of the rising permeation transient to zero permeation flux. The breakthrough method gives the following relationship[36]

$$D_{eff} = \frac{L^2}{19.8t_b}. \quad (6)$$

The so-called time-lag method is another approach where D_{eff} is obtained based on the time elapsed when the permeation flux J(t) has reached $0.63 \times J_{SS}$. This time is defined as t_{lag} and D_{eff} follows:

$$D_{eff} = \frac{L^2}{6t_{lag}}. \quad (7)$$

Another approach involves estimating D_{eff} by plotting $-\ln((J_{SS} - J(t))/J_{SS})$ versus t, which should have a gradient of $1/t_0$ where $t_0 = L^2/(\mu^2 D_{eff})$.[24] The same slope should be obtained for the decay transient when plotting $-\ln(J(t)/J_0)$ versus t, where J_0 is the current at the start of the decay transient, that is, the J_{SS} of the rising transient. Inside the materials, there may be traps with such high binding energy that the hydrogen trapped is unlikely to escape during the permeation test.[12] These traps are considered irreversible and the hydrogen trapped will not be part of the diffusible hydrogen. During the first transient, t_b and t_{lag} can be increased by the presence of irreversible traps and therefore the second transients will be used in the breakthrough and time-lag methods.

Zakroczymski[37] derived the following equation for the permeation flux on the anodic side during decay transients when both the cathodic and anodic sides of the permeation cell are under anodic polarization,

$$\frac{J(t)}{J_\infty} = 1 - \frac{2L}{(\mu D_{eff}\, t)^{1/2}} \sum_{n=0}^{\infty} \exp\left(-\frac{(2n+1)^2 L^2}{4D_{eff}\, t}\right). \quad (8)$$

D_{eff} was obtained as the value that minimized the sum of the squared error between Equation (8) and the experimental points. The first 100 terms in the series in Equation (8) were calculated. Normally, L is assumed equal to the sample thickness,[25,26] but for materials where the diffusion path of hydrogen is tortuous, a tortuosity factor can be added which relates the real diffusion distance L to the sample thickness L_0. Here, the tortuosity factor, τ, is defined as in[38]

$$\tau = \frac{L}{L_0}. \quad (9)$$

An alternative definition of tortuosity is $\omega = D_{eff}/D_\alpha$.[34] The multiple definitions can lead to confusion since a tortuous diffusion path gives $\tau > 1$ and $\omega < 1$. Using τ is more practical than ω when finding the tortuosity factor from images and was therefore chosen for this study.

3 | RESULTS

3.1 | Microstructure

The ferrite–cementite interfacial area, S_v, mean free path between particles, λ_p, and mean true spacing between lamellae, σ_0, are given in Table 3. The standard deviations of S_v, λ_p, and σ_0 depend on the standard deviation of N which was calculated assuming no

TABLE 3 Tortuosity factors, ferrite–cementite interfacial area, mean free path between cementite particles, and mean true spacing for lamellar materials, found by image analyses

Material	τ	S_v (μm^{-1})	λ_p (μm)	σ_0 (μm)
A	1.122 ± 0.036	8.521 ± 1.901	0.434 ± 0.097	N.A.
B	1.055 ± 0.010	8.022 ± 2.975	0.480 ± 0.178	N.A.
C	1.056 ± 0.022	3.066 ± 2.176	1.239 ± 0.879	N.A.
D	1.669 ± 0.266	30.761 ± 2.421	N.A.	0.065 ± 0.005
E	1.158 ± 0.015	15.237 ± 1.345	0.240 ± 0.021	N.A.
F	2.035 ± 0.344	16.758 ± 3.316	N.A.	0.119 ± 0.024

Note: Error was estimated as the standard deviation.

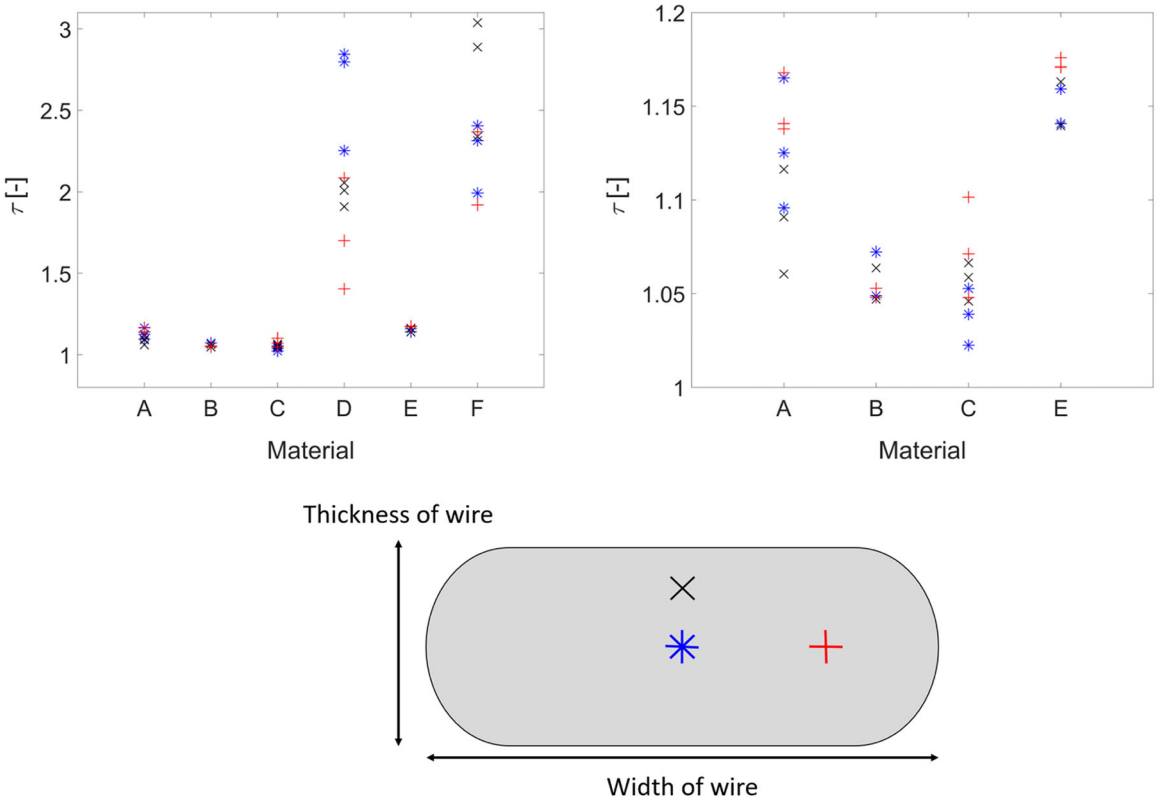

FIGURE 6 First estimation of tortuosity factors from images of ×10 000 in three different areas of the cross-sections. The areas are indicated in the lower illustration [Color figure can be viewed at wileyonlinelibrary.com]

covariance between the number of intercepts in the length, width, and thickness directions. Materials A and B had similar S_v and λ_p values despite having very different microstructures: The carbon content of A was almost twice as high as that of Material B, and Material A had ferrite grains distributed more evenly around the pearlite grains than Material B. Material C had the lowest S_v and highest λ_p while Material D had the highest S_v. Materials E and F had similar S_v, but otherwise substantially different microstructures. Material F had lamellar carbides, and ferrite grains in lines extending over 20 μm whereas Material E had a very fine microstructure with mainly small round carbides and smaller ferrite grains than Material F.

Figure 6 shows the tortuosity factors estimated for all materials with ×10 000 magnification images. The materials appeared relatively equiaxed in the width-length plane and a hydrogen diffusion obstacle was therefore considered to be equally difficult to overcome in the length as the width dimension. Hence, the 2D diffusion paths found in the images were considered representative of the 3D diffusion paths in the wire materials. The tortuosity was highest for the lamellar materials, D and F, and lowest for the materials with the lowest carbon contents and roundest

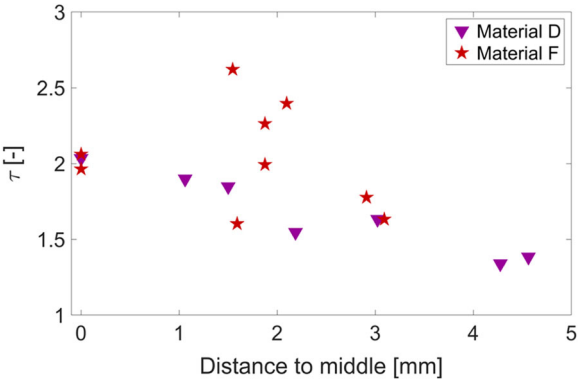

FIGURE 7 Second estimation of tortuosity factors for Materials D and F. Images of ×20 000 were used for Material D while images of ×5000 were used for Material F [Color figure can be viewed at wileyonlinelibrary.com]

carbides, B and C. The tortuosity measurements were highly scattered for Materials D and F, while they were least scattered for the materials with the finest carbide distribution, Materials B and E. For Material D, the lamellas were often blurred at ×10 000 and the evaluation of the diffusion path at this magnification was difficult. A second screening was therefore

conducted for Material D with images taken at a higher magnification. Due to the large grain size of Material F, few grains were visible in each image taken at ×10 000 magnification and the tortuosity evaluated from these images was more sensitive to grains of tortuous orientation than the evaluation of images with a higher number of grains. The tortuosity of Material F was therefore investigated again at a lower magnification. The second time the tortuosity of Materials D and F was investigated, the images were captured in several positions distributed over the cross-section at a ×20 000 magnification for Material D and ×5000 for Material F. The graph in Figure 7 displays the measured tortuosity factor versus the approximate distance to the middle of the cross-section. Notice that the distance to the middle does not represent the distance to the outer surface, since the wires have rectangular shapes with rounded corners. Material D was wider than Material F and had therefore some measurements further from the middle than Material F. At both ×10 000 and ×20 000, the tortuosity in Material D was the highest in the middle and decreased as the distance to the middle increased. For both materials, the tortuosity factor decreased when the magnifications were optimized for each of them separately. The tortuosity factors of the materials are given in Table 3.

3.2 | Electrochemical hydrogen permeation experiments

Using 0.1 M NaOH in the cathodic compartment of the hydrogen permeation cell was not ideal for the measurement of hydrogen diffusivity and hydrogen uptake in the wire materials. Before the first transient and between the first and second transients, the samples were anodically polarized on both sides and since the cathodic sides of the samples were not coated with Pd, an oxide layer can be formed on the surface, influencing diffusion.[39,40] The rising transients observed when charging carbon steel samples in 0.1 M NaOH are usually shallower than Fick's law, and this environment is therefore advised against carbon steels. More advice on charging environments for electrochemical hydrogen permeation tests can be consulted in the appendix of ISO 17081[25] and ASTM G148.[26]

The hydrogen permeation transients and decays are given in Figures 8–13. Irreversible trapping of hydrogen will give a slower diffusion during the first transient than the second transient, but the steady-state permeation currents are expected to be the same. The current of the second transients was however smaller than that of the first transients, probably as a result of oxide formation during anodic polarization on the cathode side. In this study, the oxide formation was expected to be more apparent for the second rising transient than the first, as the stabilization time before the first transient was around 24 h while the decay between the first and second transient lasted at least 3 days. The steady-state currents were estimated from the first transients since these were expected to be less affected by oxide formation on the cathodic side. However, since the current did not fully stabilize for most of the materials, the steady-state currents were defined as the current of the first transient after 93 h of exposure.

Logarithmic plots of normalized rising and decay transients are shown in Figure 14. For the rising transients, the normalized hydrogen permeation flux is $A = (J_{SS} - J(t))/J_{SS}$. For the decay transients, the normalized permeation flux of the decay transients is $A = J(t)/J_0$, where the current at the start of a decay transient, J_0, is equal to the J_{SS} of the preceding rising transient. According to Devanathan and Stachurski,[24] D_{eff} can be determined from the slope of the normalized transient:

$$\ln A = \ln 2 - \frac{\mu^2 D}{L^2} t. \tag{10}$$

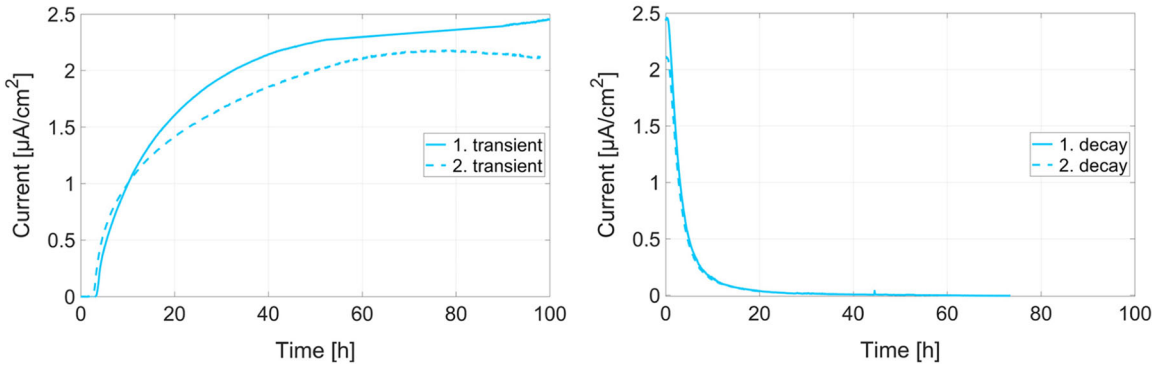

FIGURE 8 Electrochemical hydrogen permeation curves of Material A [Color figure can be viewed at wileyonlinelibrary.com]

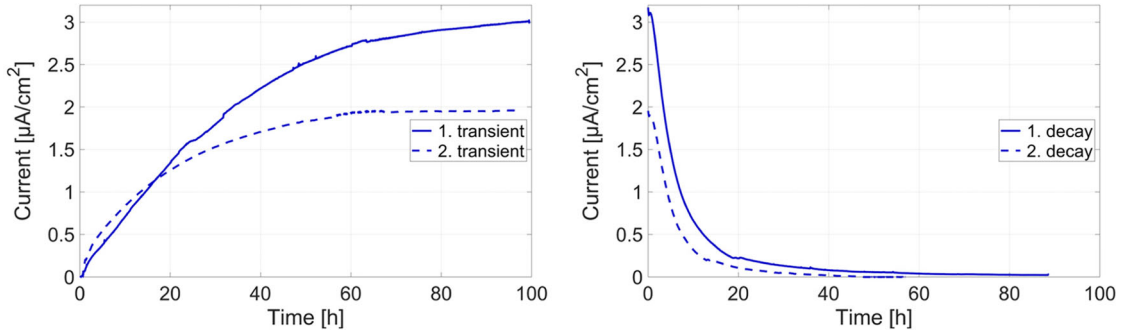

FIGURE 9 Electrochemical hydrogen permeation curves of Material B [Color figure can be viewed at wileyonlinelibrary.com]

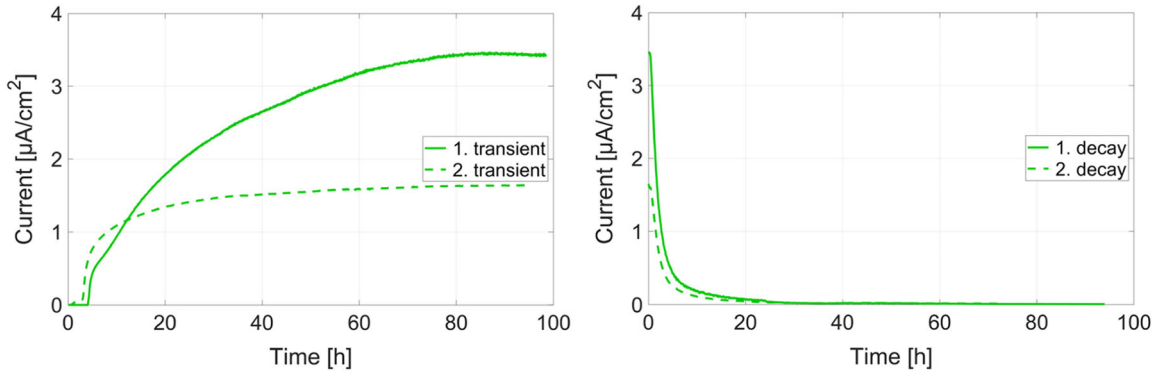

FIGURE 10 Electrochemical hydrogen permeation curves of Material C [Color figure can be viewed at wileyonlinelibrary.com]

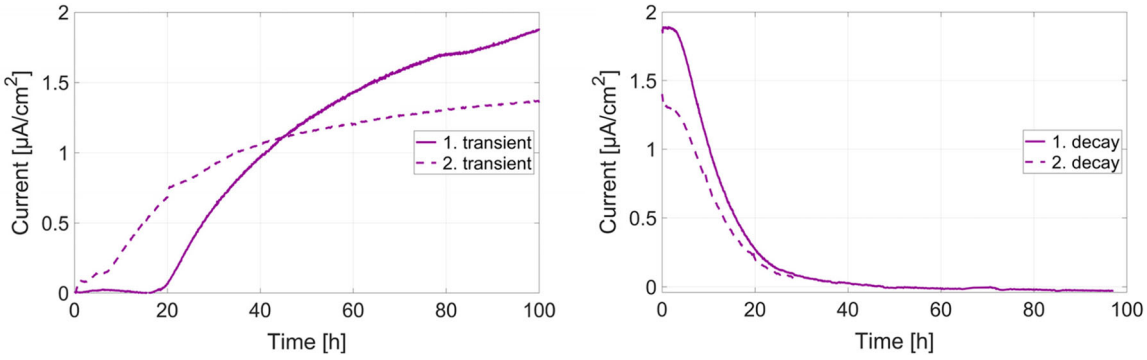

FIGURE 11 Electrochemical hydrogen permeation curves of Material D [Color figure can be viewed at wileyonlinelibrary.com]

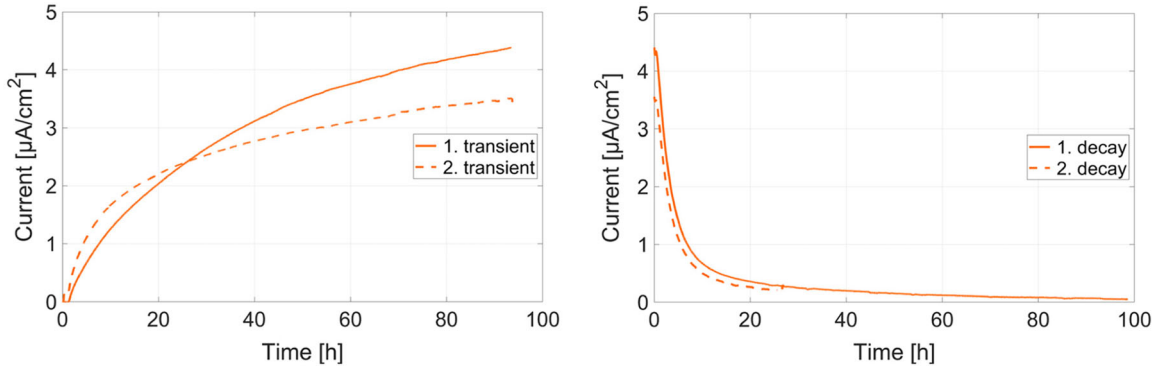

FIGURE 12 Electrochemical hydrogen permeation curves of Material E [Color figure can be viewed at wileyonlinelibrary.com]

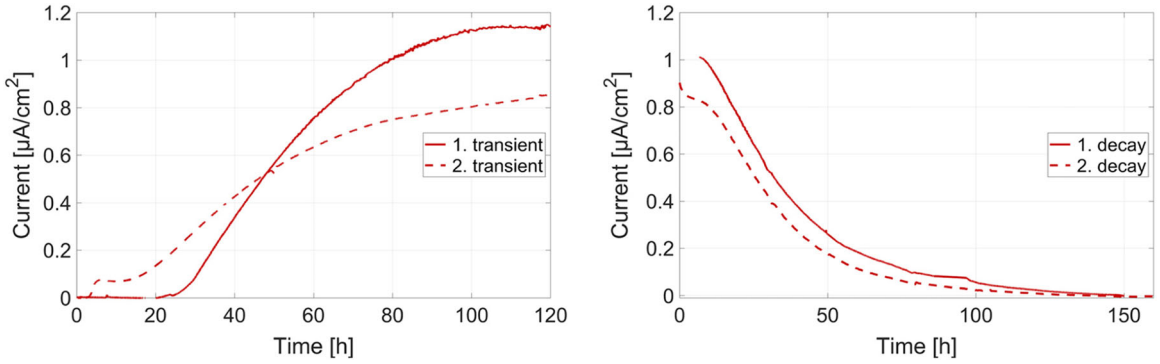

FIGURE 13 Electrochemical hydrogen permeation curves of Material F. A noisy signal was observed during the first 8 h of the first decay—these data have been removed [Color figure can be viewed at wileyonlinelibrary.com]

Notice that the decay rates in Figure 14 departed from linearity for long exposure times. The deviation from linearity could be due to the additional hydrogen diffusion out from the originally cathodic sides.[15] The diffusion coefficients were therefore estimated in the linear regions closer to the start of the decays. For Materials A, B, C, and E the linear portion of the decay occurred before 10 h, whereas the corresponding region for Material D was 10–24 h and 20–60 h for Material F. For each material, D_{eff} was calculated by several methods and the results are given in Table 4. The D_{eff} values calculated by t_{lag}, t_{b}, and slope method from the second transients differed and the reasons for this will be further elaborated in Section 4. The D_{eff} values found using the slope method on the two decay transients were consistent. An acceptable agreement was also found for D_{eff} values calculated by fitting Equation (8) to decay transients 1 and 2, and unlike the slope method, this model fitted the entire decay transient, Figure 15. The D_{eff} values calculated from the decays tended to decrease with increasing S_{v} as displayed in Figure 16.

The diffusion coefficients, D_{eff}, estimated using Equation (8) on both decay transients were used to calculate the trapped $C_{0\text{R}}$ and lattice hydrogen (C_0^{Fe}) concentrations. Equation (8) was chosen for D_{eff} calculations because the boundary conditions used in the slope method were valid only for short times while Equation (8) considers that hydrogen is removed from both sides of the sample during the decay transients and is, thus, valid throughout the duration of the decay transients, Figure 15. Lattice and reversible hydrogen concentrations are given in Table 5 along with I_{SS}, which was estimated from the current after 93 h of charging, and the normalized steady-state permeation flux $J_{\text{SS}}L$. The subsurface concentration of lattice hydrogen showed a small difference between the C_0^{av} and C_0^{Fe} values, because the volume fractions of cementite were low, Tables 1 and 5. The choice of C_0^{av} or C_0^{Fe} does not affect the ranking in lattice hydrogen concentration. $J_{\text{SS}}L$ is plotted versus λ_{p}, and σ_0 in Figure 17, showing a lack of a clear trend between permeability and cementite or platelet distance, and hence, no indication of uncompensated tortuosity effects.

4 | DISCUSSION

4.1 | Tortuosity

The effect of cementite increasing the hydrogen diffusion path in steels is often neglected in electrochemical hydrogen permeation experiments; nonetheless, several studies, especially for steels with both ferritic and austenitic phases, have shown the need to evaluate tortuosity effects of secondary phases.[12,32,34,38,41–44] For simpler, homogenous materials, the effect of tortuosity can be modeled using the grain size and shape, and orientation of the secondary phases. For example, Turnbull and Hutchings[34] estimated the tortuosity of the diffusion path by using equations originally developed in thermal transport models,[45,46] but found a 16% difference in the tortuosity factor depending on which model they used. The complexity of the microstructures in this study made it difficult to find reasonable assumptions for tortuosity models. Thus, image analyses were the preferred method, although they were affected by the choice of image magnification and the possible over or under etching of the surfaces.

The tortuosity factors found by image analyses were the lowest for Materials B and C, which had the lowest carbon contents. The tortuosity factors were about 10% higher for Materials A and E, and more than 50% higher for the lamellar materials D and F. The tortuosity of pearlitic steels has been addressed in many studies.[38,43,47] Forot et al.[38] defined the tortuosity factor as given in Equation (9) and found a tortuosity factor between 20 and 35 for fully pearlitic steel by analyzing transmission electron microscopy (TEM) micrographs. This is much higher than the tortuosity factors found for Materials D and F in this study (i.e., 1.669 and

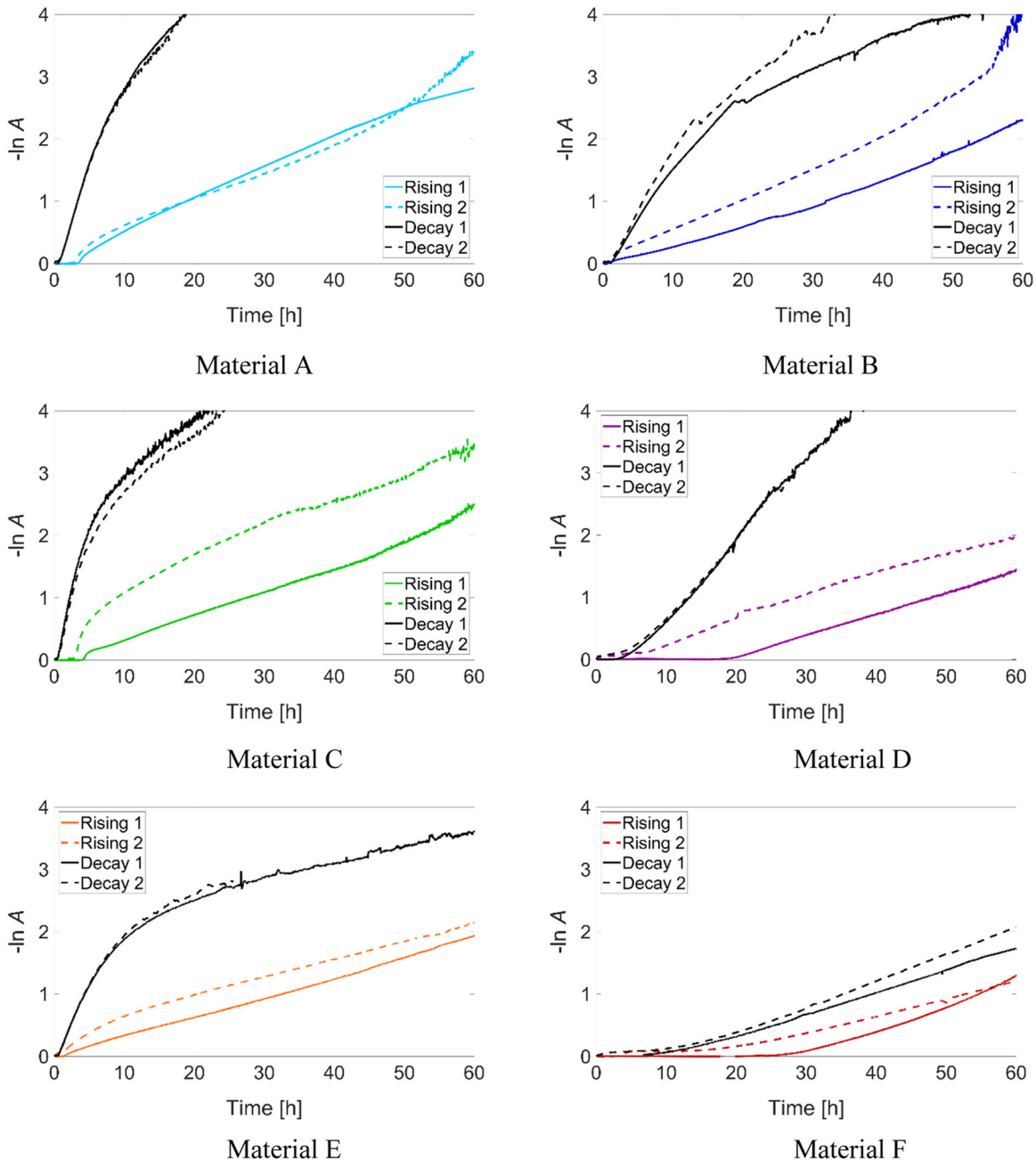

FIGURE 14 Logarithmic rise and decay plots for the electrochemical permeation tests. For the rising transient, $A = (J_{SS} - J(t))/J_{SS}$. For the decays $A = J(t)/J_0$ [Color figure can be viewed at wileyonlinelibrary.com]

2.035, respectively). Several grains in Materials D and F had discontinuous lamellas and this, in addition to the presence of ferritic grains, reduced tortuosity significantly. Another possible reason for low tortuosity factors in our work compared to Forot et al.,[38] is that the TEM images in Forot et al.[38] were obtained at a higher magnification than in our work. In this regard, as shown in Figures 6 and 7, the tortuosity factor is affected by the magnification. When the images were captured at a magnification where few grains are seen in each image, the perceived possible diffusion paths will mainly go through the grain interior, whereas using images of lower magnification allows for seeing diffusion paths along grain boundaries. As we will show in the discussion of the steady-state permeation flux, it is likely that diffusion is occurring on the grain boundaries, supporting the choice of using the tortuosity measured at lower magnifications as long as the discontinuities of the lamellas are still visible. The tortuosity factor of the lamellar materials had the highest standard deviations, which was expected since tortuosity measurements are strongly affected by the orientation of any lamellar grains. The lowest standard deviations were found for Materials B and E, which are the

TABLE 4 D_{eff} calculated with different methods for the second rising and the decay transients

Material	Using the second transient			Using decays			
	D_{eff} (tb) ($cm^2\ s^{-1}$)	D_{eff} (tlag) ($cm^2\ s^{-1}$)	D_{eff} (slope) ($cm^2\ s^{-1}$)	D_{eff} (slope, decay 1) ($cm^2\ s^{-1}$)	D_{eff} (slope, decay 2) ($cm^2\ s^{-1}$)	D_{eff} (Equation 8, decay 1) ($cm^2\ s^{-1}$)	D_{eff} (Equation 8, decay 2) ($cm^2 s^{-1}$)
A	4.20×10^{-7}	2.11×10^{-7}	9.17×10^{-8}	9.06×10^{-7}	9.11×10^{-7}	1.19×10^{-6}	1.16×10^{-6}
B	2.15×10^{-6}	2.23×10^{-7}	1.25×10^{-7}	4.93×10^{-7}	5.22×10^{-7}	7.55×10^{-7}	7.42×10^{-7}
C	3.99×10^{-7}	4.46×10^{-7}	1.33×10^{-7}	1.28×10^{-6}	1.22×10^{-6}	1.81×10^{-6}	1.59×10^{-6}
D	6.48×10^{-7}	3.02×10^{-7}	1.56×10^{-7}	5.94×10^{-7}	6.17×10^{-7}	6.62×10^{-7}	6.59×10^{-7}
E	1.51×10^{-6}	2.01×10^{-7}	7.27×10^{-8}	6.61×10^{-7}	6.92×10^{-7}	9.73×10^{-7}	1.09×10^{-6}
F	3.99×10^{-7}	3.10×10^{-7}	2.60×10^{-7}	2.64×10^{-7}	2.75×10^{-7}	4.01×10^{-7}	4.29×10^{-7}

Note: The tortuosity factors in Table 3 were used to estimate the real hydrogen diffusion distance required for D_{eff} calculations.

materials with the finest carbides and the most homogenous carbide distribution. In the following discussion, the tortuosity factor is used for all materials unless otherwise stated.

4.2 | Diffusion coefficient

The D_{eff} values calculated using the decay transients gave relatively reproducible results. The use of the decay transients for estimating the diffusion coefficient is less common than using the second rising transients since the boundary conditions are harder to define during the decay.[48] However, the hydrogen concentration at the previous entry side is fixed to zero by applying an anodic potential on the previous hydrogen entry side during decay transients.[25,26,48] The hydrogen entry side was not coated with Pd, which can lead to less efficient desorption of hydrogen there compared to the hydrogen exit side and a gentler slope than Equation (8) predicts. A gentler slope is observed for the materials with globular carbides, see Figure 15, and less efficient hydrogen desorption on the hydrogen entry side may have caused this. It is, however, interesting that this has not affected Material D which was charged with hydrogen for as long as Materials A and B. When using the rising transients for calculating D_{eff} (the breakthrough, time lag, and slope methods) the results were inconsistent and often one order of magnitude lower than the diffusion coefficients calculated by the slope method for the decays. The time lag method is dependent on the steady-state current and the D_{eff} will be erroneous if the steady-state current is not achieved. This may have happened to the materials that did not reach steady state during the rising transients. A difference in D_{eff} calculated by different methods can indicate that D_{eff} is dependent on the hydrogen concentration, but the difference can also be related to oxide formation on the cathodic side of the sample when this side is anodically polarized. Zakroczymski[39] explained how the oxide formed on the cathode side of a permeation test sample during exposure to 0.1 M NaOH impedes diffusion, leading to erroneous results. The thickness of the oxide will decrease during charging, and the D_{eff} calculated by the breakthrough method is, therefore, likely to be more affected than the D_{eff} calculated by the time-lag method.[49] Zakroczymski and Szklarska-Smialowska[40] showed that the oxide effect can be reduced by charging the sample for 90 h before partial permeation decay and rising transients to estimate D_{eff}. In our work, the steel surfaces were charged for a minimum of 93 h before the decay, but instead of doing a series of partial decay and rising transients, the decay was kept until a steady state was reached. The first decays were kept for a minimum of 73 h before a new transient was measured. During the decay, the surface changes, and the longer the decay lasts, the longer it will take for the current to reach a steady state again.[39] This can explain why Material A, which had the shortest first decay, was the material where the second transient was closest to reaching the same current density as the first transient. The other materials had at least 96 h of decay between the two transients. The current densities in the second transients did not reach the same magnitude as the current densities in the first transients, but this does not appear to affect the diffusion coefficients calculated with the decays. The second decays gave D_{eff} values with less than 14% deviation from those calculated from the first decays. Materials A, B, and D had the lowest deviations, below 3%.

All the equations for D_{eff} used in this paper are based on the assumption that Fick's second law is applicable. For the rising transients, it appears that the oxide formation interferes with the hydrogen flux and makes the

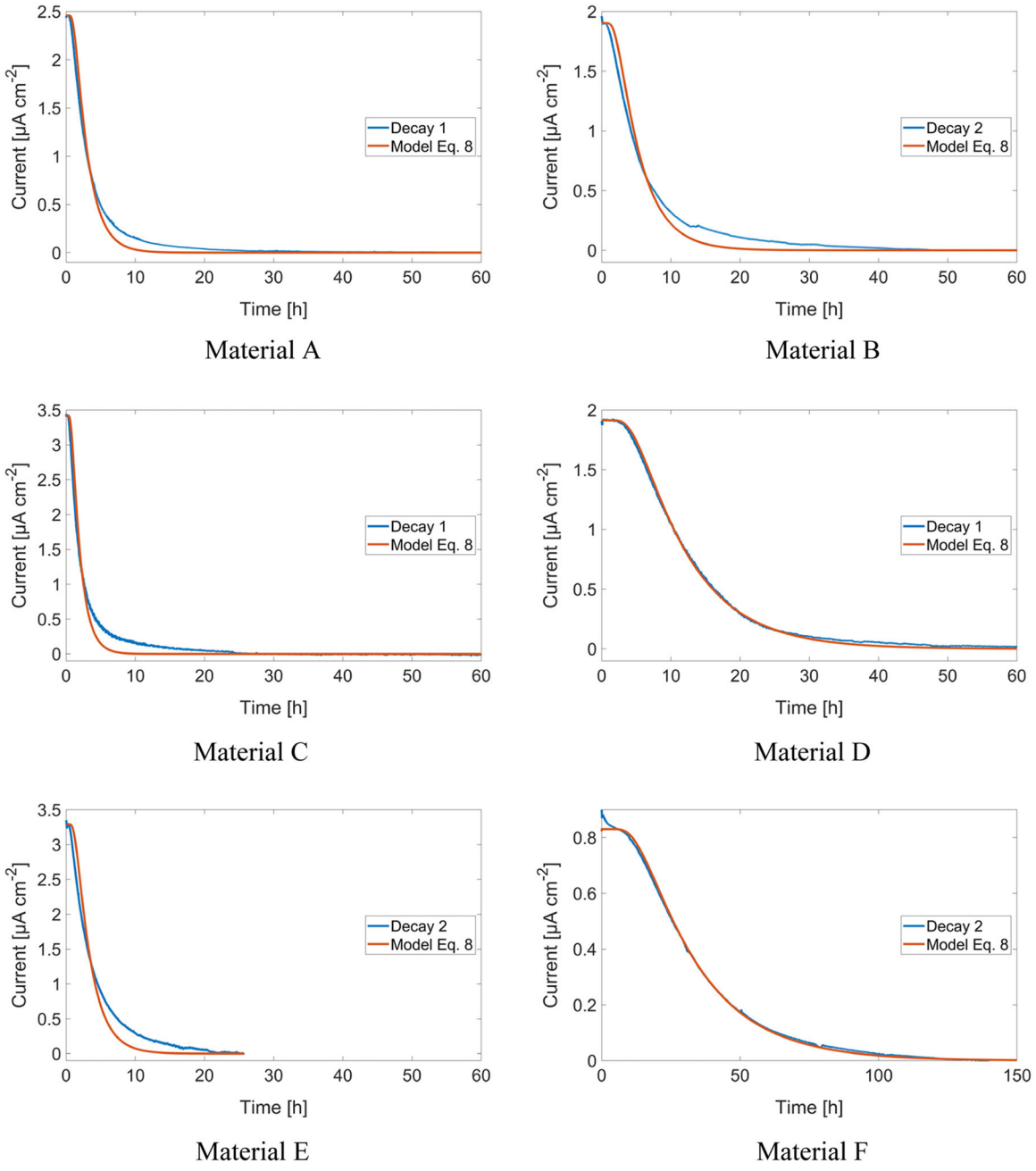

FIGURE 15 Hydrogen permeation decay transients and fitted Equation (8). For each material, the decay with the best fit is displayed [Color figure can be viewed at wileyonlinelibrary.com]

D_{eff} calculations invalid. For the decays, the models fitted using Equation (8) showed a good fit with most of the decay transients, Figure 15. The fit was best for Materials D and F, and least good for Materials B and E which had slightly less steep transients than what Equation (8) predicts. This indicates that oxides on the hydrogen entry side were slightly affecting the permeation during the decay transients for these two materials. The relatively good fit between decay transients and the fitted models indicates that D_{eff} is not dependent on the hydrogen concentration in the material and that Fick's second law is applicable for the decays. When D_{eff} is dependent on trap occupancy, it will increase as the trap occupancy increases and the transients will show a steeper transient than the fitted models.[12] The trap occupancy decreases with time during the decay transients, meaning that the hydrogen trap occupancy is higher for the data used in the slope method for decays than it is for the datasets fitted to Equation (8). The D_{eff} values found using the slope method on the decays were 6%–37% lower than the

D_{eff} values found by curve fitting, which shows that D_{eff} was increasing with decreasing trap occupancy. This is an indication of unsteady surface conditions,[26] and can be related to the oxides on the cathodic side, although the relatively good fit with Equation (8) shows that unsteady state conditions do not appear to have decreased the fit so strongly. Despite the uncertainty of the D_{eff} values, it is considered useful to compare the D_{eff} of different materials when the D_{eff} values have been calculated in the same manner.[12] When different methods give different D_{eff} values, it can be reasonable to choose the highest D_{eff} since the permeation transients cannot outrun the diffusion.[14,50] D_{eff} found by model fitting to Equation (8) is therefore considered most reliable to use for C_{OR} calculations and for comparing the diffusivity of the materials.

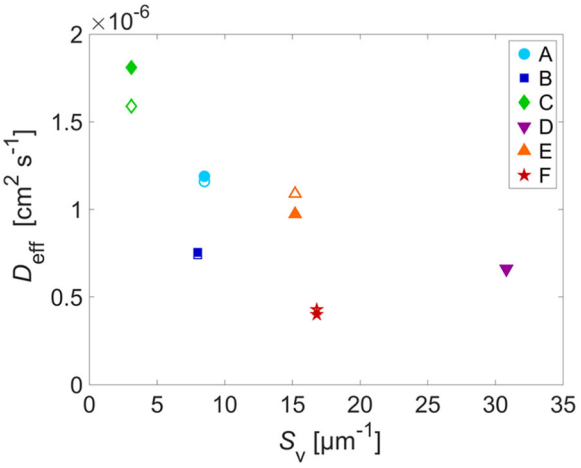

FIGURE 16 D_{eff} of the various wire materials calculated by fitting Equation (8) to the hydrogen permeation decay transients versus the estimated ferrite–cementite interfacial area. D_{eff} values from the first decay transients are shown as filled symbols while D_{eff} values from the second decay transients are shown as unfilled symbols. The tortuosity factor was used for all materials [Color figure can be viewed at wileyonlinelibrary.com]

The D_{eff} values calculated from fitting Equation (8) to the decay transients were plotted against the estimated ferrite–cementite interfacial area in Figure 16. The graphs show that D_{eff} decreased as S_v increased, which is expected to increase hydrogen trapping on ferrite–cementite interfaces.[15] In contrast, Materials B and F had relatively low D_{eff} values compared to the wire materials with similar S_v. Bott et al.[51] discussed the influence of coherency between the ferrite and cementite for the hydrogen trapping in the ferrite–cementite interfaces by conducting hydrogen permeation tests on low-carbon steel heat-treated in three different ways to form a sample consisting of ferrite and pearlite, a sample with spheroidized cementite, and an aged sample with very fine carbide particles. The ferritic–pearlitic steel sample had the highest hydrogen diffusivity, the spheroidized sample showed an intermediate value, and the aged microstructure had the lowest hydrogen diffusivity. The low diffusivity of the steel in the aged condition was attributed to the compressive stress fields surrounding the dispersed particles, which were about 20 nm in diameter and had high coherency to the ferrite matrix. The globular cementite exhibited mainly incoherent carbide–cementite interfaces which gave a lower hydrogen diffusivity and higher hydrogen uptake than the pearlitic microstructure. Both small particles of size approximately 20 nm and larger globular particles were seen for Materials A, B, C, and E studied in this study, but the size distribution of the carbides has not been characterized. Bott et al.[51] suggested that the high diffusivity in the ferritic–pearlitic microstructure indicated that the proeutectoid ferrite on the grain boundaries is the preferential hydrogen diffusion path. This hypothesis is consistent with the observed diffusion coefficients for the lamellar materials in our work: The grain size of Material F was larger than that of Material D and the D_{eff} of Material F lower than that of Material D. The estimation of the tortuosity factors conducted herein considered only what appears to be the shortest diffusion path and did not take into consideration whether some

TABLE 5 Results from the electrochemical hydrogen permeation tests

Material	$J_{SS}L$ (mol cm^{-1} s^{-1})	$J_{SS}^{Fe}L$ (mol cm^{-1} s^{-1})	C_{0R} (using D_{eff} from Equation 8, decay 1) (ppmw)	C_{0R} (using D_{eff} from Equation 8, decay 2) (ppmw)	C_0^{av} (Equation 1) (ppmw)	C_0^{Fe} (Equation 2) (ppmw)
A	7.25×10^{-12}	7.85×10^{-12}	0.69	0.71	0.0127	0.0138
B	9.41×10^{-12}	9.83×10^{-12}	1.59	1.62	0.0165	0.0171
C	1.03×10^{-11}	1.09×10^{-11}	0.73	0.83	0.0181	0.0191
D	7.99×10^{-12}	9.15×10^{-12}	1.54	1.55	0.0140	0.0157
E	1.33×10^{-11}	1.47×10^{-11}	1.74	1.55	0.0233	0.0255
F	6.59×10^{-12}	7.32×10^{-12}	2.09	1.96	0.0115	0.0126

Note: The tortuosity factors in Table 3 were used in the calculations to estimate the real hydrogen diffusion distance.

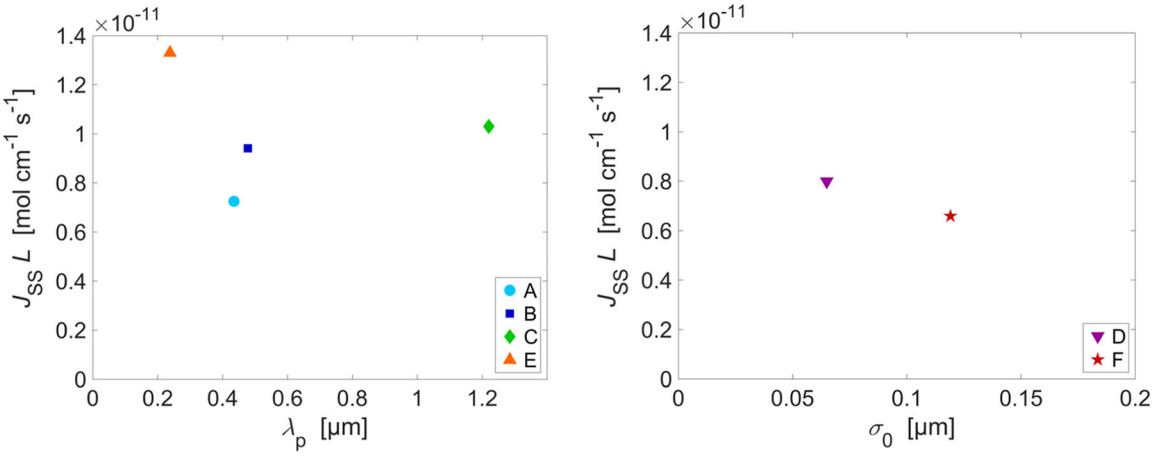

FIGURE 17 Steady-state hydrogen permeation flux versus mean free path between cementite particles for the microstructures with round carbides and versus true mean spacing for the lamellar materials. The tortuosity factor was used in the calculations [Color figure can be viewed at wileyonlinelibrary.com]

paths, for example, grain boundaries, might be preferential for diffusion. The relation between the D_{eff} values and grain sizes of Materials D and F suggested that the estimated tortuosity factor did not correlate with the shortest hydrogen diffusion path in the lamellar materials, but other factors might also affect D_{eff}.

Plastic deformation can affect D_{eff}, as the increased number of dislocations, and hence trapping sites, results in a lower diffusion coefficient.[16–19,52] All the wire materials have grain shapes that indicate plastic deformation, but Materials A and C appeared to be less deformed than the rest. This agrees with the higher D_{eff} values displayed by these materials in comparison with the other materials.

4.3 | Normalized steady-state permeation flux and lattice hydrogen uptake

The normalized steady-state permeation fluxes measured for the materials tended to increase as the grain size decreased. Materials A and F had the largest grain sizes and the lowest $J_{SS}L$ values, while the material with the smallest ferrite grains, that is, Material E, had the highest $J_{SS}L$ value. This can indicate hydrogen trapping on the grain boundaries, but this is questionable since the diffusion coefficients did not decrease with the grain size. Another possibility is that the proeutectoid ferrite is a preferential diffusion path, leading to a tortuosity effect that has not been compensated for.

The steady-state permeation flux is also known to be affected by cold work. Riecke[53] measured the steady-state permeation flux of iron and several steels in recrystallized and cold-worked conditions. For ferrite, the steady-state permeation flux for recrystallized microstructure was the same as 80% cold-worked ferrite. This is in line with the models that consider that trapping should not affect the steady-state permeation flux.[25,26] For fine pearlite, the steady-state flux was not affected by 15% cold work, but 37% cold work led to a decrease in the steady-state permeation flux.[53] Jeng et al.[20] compared the electrochemical hydrogen permeation parameters for pearlitic steels with the same composition and grain size, but different interlamellar spacing. The steady-state flux was the highest for a coarse pearlite microstructure, intermediate for medium pearlite, and the lowest for fine pearlite steel. The observations of both Riecke[53] and Jeng et al.[20] may be related to an increased tortuosity of the hydrogen diffusion path, due to an increased number of obstacles or due to lamellas orienting themselves in the rolling direction. Such a preferential lamella orientation is seen for Material D in our work, Figure 2, and is also indirectly displayed in how the tortuosity of Material D is highest in the middle of the wire, see Figure 7. This trend was not evident for Material F, which had a lower plastic deformation than Material D (i.e., compare the grains in Figure 1) and had a coarser pearlite phase.

There are several studies on how heat treatments affect the steady-state permeation flux. The studies by Luu and Wu[33] on the hydrogen permeation through medium carbon steel with different heat treatments showed that normalized, annealed, and spheroidized microstructures had similar steady-state permeation rates, while the steady-state permeation rate of a quenched martensitic microstructure

was about 50% lower. Similar observations were found by Johnson and Wu.[15] When comparing microstructures, the authors found that the steels with spheroidized carbides had the highest hydrogen permeation flux, while the quenched and tempered microstructure had the lowest one. The same authors found that the hydrogen permeation flux increased with increasing interparticle spacing and decreased as the carbide volume fraction increased by studying annealed steels in more detail. The increase in hydrogen permeation flux with pearlite spacing can be related to increased tortuosity, as discussed above.

Johnson and Krauss[13] found that the steady-state permeation flux increased linearly with the interparticle spacing for austenitized, quenched, and spheroidized AISI 1050 steel samples where only the spheroidizing time varied from sample to sample. However, when testing a sample of the same alloy without the quenching step, the permeation flux was reduced in half. Both microstructures were described as spheroidized carbides and ferrite, and the interparticle spacing, particle radius, and interfacial carbide area were similar for the two materials. Thus, quenching in itself appears to reduce the steady-state hydrogen permeation flux, but a subsequent spheroidizing step increases the steady-state permeation. Possibly, the high permeation rate of the quenched and spheroidized material observed by Johnson and Krauss[13] is related to a smaller grain size associated with additional quenching steps in the production. However, this could not be confirmed since the authors provided no information about the grain sizes of the two materials. In this study, the hydrogen permeation flux did not increase with increasing interparticle spacing and interlamellar spacing, as is shown in Figure 17. In Figure 17, the tortuosity factor was taken into consideration, but even without this factor, there was no clear trend between permeation flux and interparticle or interlamellar spacing. There was no trend between $J_{SS}^{Fe}L$ and the interparticle or interlamellar spacing either, Table 5. This shows that the interparticle and interlamellar spacing had no clear effect on the normalized hydrogen permeation fluxes of the carbon steels when several parameters, like thermomechanical processing and chemical composition, were varied.

4.4 | Hydrogen uptake

The hydrogen uptake in lattice and reversible sites, C_{0R}, was calculated using Equation (5) with D_{eff} from Equation (8) using both the first and second decay transients. C_{0R} is therefore directly linked to the steady-state permeation flux and diffusion coefficients discussed in the previous sections. The relationship between D_{eff} and S_v suggested considerable hydrogen trapping on ferrite–cementite grain boundaries and the $J_{SS}L$ values showed higher hydrogen uptakes as the grain size decreased; nevertheless, C_{0R} did not follow either of these trends. C_{0R} was the lowest for Materials A and C, and about twice as high for Materials B, D, E, and F. The differences in C_{0R} may be related to plastic deformation since Materials A and C appeared less deformed than the others.

The effect of plastic deformation on the HE of iron and carbon steels has been the subject of several studies.[16–19,21,28,52,54–56] Deformation is expected to affect permeation by increasing the density of trapping sites like microvoids, vacancy clusters, and dislocations.[16–18,52] Ha et al.[18] performed electrochemical permeation tests of cold-worked steels and found that the trap density increased almost 10-fold when the material was subject to 10% reduction. The results also showed that the trap density increased by rolling while the trap occupancy was not altered. Nagumo et al.[17] used thermal desorption spectroscopy to compare the hydrogen uptake of eutectoid steel and found four times higher hydrogen uptake for material with 25% drawing reduction compared to the same material with 0% drawing reduction. The microstructure of the steel consisted of fine lamellas of cementite and ferrite with a spacing of 60 nm, which is similar to the microstructure of Material D in this study. After annealing, the amount of hydrogen substantially decreased. The hydrogen uptake decreased from 8 to 3 ppmw for samples annealed at 600°C. Even at annealing temperatures where the hardness of the material was just slightly affected, the hydrogen uptake decreased by about 25%. From the microstructure images in Figure 1, Materials A and C appeared less deformed while Materials B, D, and E had a more deformed microstructure. This indicates that the deformation plays a more important role in the relative hydrogen uptakes of the steel wires than the grain size and ferrite–cementite interface area.

5 | CONCLUSION

This paper compared the electrochemical hydrogen permeation experiments of materials used in industrial components as a function of microstructure. The tortuosity of the hydrogen diffusion path in the materials was estimated by analyzing SEM micrographs. The calculated tortuosity, multiplied by the membrane thickness, yielded the real diffusion distance required for subsequent analyses.

The electrochemical permeation tests were conducted with 0.1 M NaOH in the hydrogen charging environment. This is not recommended for carbon steels, as the rising transients in this environment are usually affected by the formation of oxides on the surface. The decay transients

were less affected by the unstable surface conditions on the hydrogen entry side and were used for the estimation of effective diffusion coefficients.

Several factors affecting hydrogen transport properties were investigated, such as plastic deformation introduced by cold-work, carbide content and distribution, and heat treatments. After compensating for the tortuosity of the hydrogen diffusion path, the hydrogen permeation flux increased with decreasing grain size, but hydrogen trapping on the grain boundaries could not be confirmed by the measured diffusion coefficients. Another possible explanation for the trend between normalized hydrogen permeation flux and grain size is that proeutectoid ferrite may be a preferential hydrogen diffusion path, leading to a tortuosity effect that was not compensated for. The normalized steady-state flux ranged from 6.6 to 7.3×10^{-12} mol cm^{-1} s^{-1} for the materials with the largest grain sizes to 1.3×10^{-11} mol cm^{-1} s^{-1} for the material with the smallest ferrite grain size.

The effective diffusion coefficients were mainly affected by the hydrogen trapping on the ferrite–cementite interfaces. It was also evident that the materials with the lowest amount of plastic deformation had the highest diffusion coefficients. The effective diffusion coefficients ranged from 4.0×10^{-7} to 1.8×10^{-6} cm^2 s^{-1}.

Overall, the most deformed microstructures displayed the highest hydrogen uptake. In this regard, the two materials with less deformed microstructures had hydrogen uptakes in the order of 0.7 ppmw, while the more deformed microstructures had hydrogen uptakes ranging from 1.5 to 2.1 ppmw.

ACKNOWLEDGMENTS

This study was performed as part of the KPN project "Environmental Cracking of Flexible Pipe Armour Wires," Research Council of Norway Project No. 280760 within the PETROMAKS 2 program. The authors would like to thank the following project participants for financial and technical support: The Research Council of Norway, Equinor, Shell, Chevron, Petrobras, OKEA, TechnipFMC, NOV, Baker Hughes, and 4Subsea.

CONFLICT OF INTERESTS

The authors declare that there are no conflict of interests.

DATA AVAILABILITY STATEMENT

The data that support the findings of this study are available from the corresponding author upon reasonable request.

ORCID

Ellen S. Skilbred https://orcid.org/0000-0001-6674-3972
Roy Johnsen http://orcid.org/0000-0002-5449-7396

REFERENCES

[1] E. Remita, F. Ropital, J. Kittel, B. Tribollet, E. Sutter, C. Taravel-Condat, N. Desamais, *CORROSION* 2008, New Orleans, LA **2008**, 4737.
[2] A. Rubin, M. H. Haarh, S. Overby, T. S. Nielsen, J. Gudme, *CORROSION 2012*, Salt Lake City, Utah **2012**, 4002.
[3] A. Dugstad, S. Palencsár, T. Berntsen, L. Børvik, *SPE International Oilfield Corrosion Conference and Exhibition*, Aberdeen, Scotland **2018**, 1.
[4] Y. Makino, T. Okamoto, Y. Goto, M. Araki, *Offshore Technology Conference*, Houston, TX **1988**, 537.
[5] 4subsea/PSA-Norway Report no. 0389-26583-U-0032, *Unbonded Flexible Risers – Recent Field Experience and Actions for Increased Robustness*, 4Subsea AS, Nesbru, Norway **2013**.
[6] M. J. Al-Maslamani, *Offshore Technology Conference*, Houston, Texas **1996**, 213.
[7] D. Pipa, S. Morikawa, G. Pires, C. Camerini, J. M. Santos, *EURASIP J. Adv. Signal Process.* **2010**, *2010*, 176203.
[8] NACE/ASTM G193-20a NACE International, Houston, TX/ASTM International, West Conshohocken, PA **2020**.
[9] S. Lynch, *Corros. Rev.* **2012**, *30*, 105.
[10] P. Kedzierzawski, in *Hydrogen Degradation of Ferrous Alloys*, 4th ed. (Eds: R. A. Oriani, J. P. Hirth, M. Smialowski), William Andrew Publishing/Noyes **1985**, p.271.
[11] K. O. Findley, M. K. O'Brien, H. Nako, *Mater. Sci. Technol.* **2015**, *31*, 1673.
[12] A. Turnbull, *Int. J. Hydrogen Energy* **2015**, *40*, 16961.
[13] D. Johnson, G. Krauss, *Metall. Trans. A* **1987**, *18A*, 717.
[14] H. Husby, M. Iannuzzi, R. Johnsen, M. Kappes, A. Barnoush, *Int. J. Hydrogen Energy* **2018**, *43*, 3845.
[15] D. L. Johnson, J. K. Wu, *J. Mater. Energy Syst.* **1987**, *8*, 402.
[16] A. J. Kumnick, H. H. Johnson, *Metall. Mater. Trans. B* **1974**, *5*, 1199.
[17] M. Nagumo, K. Takai, N. Okuda, *J. Alloys Compd.* **1999**, *293–295*, 310.
[18] H. M. Ha, J.-H. Ai, J. R. Scully, *Corrosion* **2014**, *70*, 166.
[19] H.-J. Kim, H.-Y. Jung, T.-W. Kwon, Y.-D. Chung, *Mater. Trans.* **2019**, *60*, 1614.
[20] H. W. Jeng, L. H. Chiu, D. L. Johnson, J. K. Wu, *Metall. Mater. Trans. A* **1990**, *21A*, 3257.
[21] H. Izadi, M. Tavakoli, M. H. Moayed, *Mater. Chem. Phys.* **2018**, *220*, 360.
[22] API Specification 17J, *Specification for Un*bonded Flexible Pipe, American Petroleum Institute, Washington, DC **2014**.
[23] NACE Standard TM0198, NACE International, Houston, TX **2016**.
[24] M. A. V. Devanathan, Z. Stachurski, *Proc. R. Soc. London, Ser. A* **1962**, *270*, 90.
[25] ISO 17081, *Method of measurement of hydrogen permeation and determination of hydrogen uptake and transport in metals by an electrochemical technique*, International Organization for Standardization, Geneva, Switzerland **2014**.
[26] ASTM G148, Standard Practice for Evaluation of Hydrogen Uptake, Permeation, and Transport in Metals by an Electrochemical Technique, ASTM, West Conshohocken, PA **2018**.
[27] P. Bruzzoni, *Ph.D. Thesis*, Universidad de Buenos Aires, **2003**.
[28] P. C. Rivera, V. P. Ramunni, P. Bruzzoni, *Corros. Sci.* **2012**, *54*, 106.
[29] P. Bruzzoni, R. Garavaglia, *Corros. Sci.* **1992**, *33*, 1797.

[30] P. Manolatos, M. Jerome, J. Galland, *Electrochim. Acta* **1995**, *40*, 867.
[31] A. J. Haq, K. Muzaka, D. P. Dunne, A. Calka, E. V. Pereloma, *Int. J. Hydrogen Energy* **2013**, *38*, 2544.
[32] G. M. Pressouyre, *Metall. Mater. Trans. A* **1983**, *14*, 2189.
[33] W. C. Luu, J. K. Wu, *Corros. Sci.* **1996**, *38*, 239.
[34] A. Turnbull, R. B. Hutchings, *Mater. Sci. Eng., A* **1994**, *177*, 161.
[35] K. Kiuchi, R. B. McLellan, *Acta Metall.* **1983**, *31*, 961.
[36] S. Frappart, X. Feaugas, J. Creus, F. Thebault, L. Delattre, H. Marchebois, *J. Phys. Chem. Solids* **2010**, *71*, 1467.
[37] T. Zakroczymski, *J. Electroanal. Chem.* **1999**, *475*, 82.
[38] C. Forot, E. Legrand, E. Roguet, J. Creus, J. Kittel, X. Feaugas, *Eurocorr 2015*, Graz, Austria **2015**, p.107.
[39] T. Zakroczymski, *Scr. Metall.* **1985**, *19*, 521.
[40] T. Zakroczymski, Z. Szklarska-Smialowska, *J. Electrochem. Soc.* **1985**, *132*, 2548.
[41] E. Owczarek, T. Zakroczymski, *Acta Mater.* **2000**, *48*, 3059.
[42] T. Zakroczymski, E. Owczarek, *Acta Mater.* **2002**, *50*, 2701.
[43] A. Turk, S. Pu, D. Bombač, P. E. J. Rivera-Díaz-del-Castillo, E. I. Galindo-Nava, *Acta Mater.* **2020**, *197*, 253.
[44] V. Olden, C. Thaulow, R. Johnsen, *Mater. Des.* **2008**, *29*, 1934.
[45] D. P. H. Hasselman, L. F. Johnson, *J. Compos. Mater.* **1987**, *21*, 508.
[46] L. E. Nielsen, *Ind. Eng. Chem. Fundam.* **1974**, *13*, 17.
[47] L. Tau, S. L. I. Chan, *Mater. Lett.* **1996**, *29*, 143.
[48] J. McBreen, L. Nanis, W. Beck, *J. Electrochem. Soc.* **1966**, *113*, 1218.
[49] N. Boes, H. Züchner, *J. Less-Common Met.* **1976**, *49*, 223.
[50] J. P. Hirth, *Metall. Trans. A* **1980**, *11*, 861.
[51] A. H. Bott, D. S. Dos Santos, P. E. V. De Miranda, *J. Mater. Sci. Lett.* **1993**, *12*, 390.
[52] A. J. Kumnick, H. H. Johnson, *Acta Metall.* **1980**, *28*, 33.
[53] E. Riecke, *Werkst. Korros.* **1981**, *32*, 66.
[54] M. L. Hill, E. W. Johnson, *Trans. Metall. Soc. AIME* **1960**, *215*, 717.
[55] W. Dietzel, M. Pfuff, G. G. Juilfs, *Mater. Sci.* **2006**, *42*, 78.
[56] E. Van den Eeckhout, A. Laureys, Y. Van Ingelgem, K. Verbeken, *Mater. Sci. Technol.* **2017**, *33*, 1515.

How to cite this article: E. S. Skilbred, M. Kappes, M. Iannuzzi, R. Johnsen, *Mater. Corros.* **2021**, 1–20. https://doi.org/10.1002/maco.202112615